

A Deep Learning Approach for Automatic Scoliosis Cobb Angle Identification

Renato R. Maaliw III
College of Engineering
Southern Luzon State University
Lucban, Quezon, Philippines
rmaaliw@slsu.edu.ph

Julie Ann B. Susa
College of Engineering
Southern Luzon State University
Lucban, Quezon, Philippines
jsusa@slsu.edu.ph

Alvin S. Alon
Digital Transformation Center
Batangas State University
Batangas City, Philippines
alvin.alon@g.batstate-u.edu.ph

Ace C. Lagman
Information Technology Dept.
FEU Institute of Technology
Manila, Philippines
aclagman@feutech.edu.ph

Shaneth C. Ambat
Information Technology Dept.
FEU Institute of Technology
Manila, Philippines
scambat@feutech.edu.ph

Manuel B. Garcia
Information Technology Dept.
FEU Institute of Technology
Manila, Philippines
mbgarcia@feutech.edu.ph

Keno C. Piad
Information Technology Dept.
Bulacan State University
Malolos, Bulacan, Philippines
keno.piad@bulsu.edu.ph

Ma. Corazon Fernando - Raguro
Information Technology Dept.
FEU Institute of Technology
Manila, Philippines
mgfernando@feutech.edu.ph

Abstract—Efficient and reliable medical image analysis is indispensable in modern healthcare settings. The conventional approaches in diagnostics and evaluations from a mere picture are complex. It often leads to subjectivity due to experts' various experiences and expertise. Using convolutional neural networks, we proposed an end-to-end pipeline for automatic Cobb angle measurement to pinpoint scoliosis severity. Our results show that the Residual U-Net architecture provides vertebrae average segmentation accuracy of 92.95% based on Dice and Jaccard similarity coefficients. Furthermore, a comparative benchmark between physician's measurement and our machine-driven approach produces an acceptable mean deviation of 1.57 degrees and a T-test p-value of 0.9028, indicating no significant difference. This study has the potential to help doctors in prompt scoliosis magnitude assessments.

Keywords—computer vision, image processing, neural network, machine learning, medical diagnosis, x-ray

I. INTRODUCTION

The spine is a critical part of the body providing structural support and performs numerous essential roles, such as bearing the body's weight and safeguarding the spinal cord. It is composed of 33 vertebrae, divided into five sections, cervical (C), thoracic (T), lumbar (L), sacrum (S) & coccyx (Co) [1]. Scoliosis is a malformation of the spine characterized by lateral curvature that most commonly occurs during a person's development spurt before adolescence [2]. It can occur before the complete evolution of the skeleton as it impacts the body's structure, cardiopulmonary function, and even paralysis or immobility. According to statistics, its prevalence is approximately 470 to 5,200 per 100,000 individuals worldwide, most commonly among 9 to 15 years old [3].

However, while most scoliosis instances are modest with no known cause, various spine abnormalities may increase as an individual grows, and specific types of the condition can be severely crippling in some situations. In extreme contexts, such as when the spinal curve is severe, it reduces the amount of room available in the chest, making it more difficult for the lung to function correctly and poses a risk of additional organ damage. Figure 1 shows a normal and an abnormal spine based on curvature.

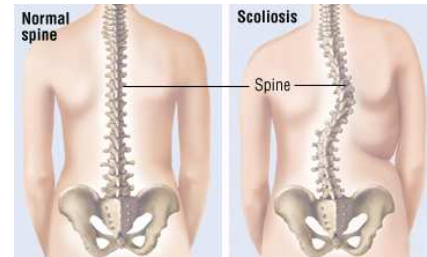


Fig. 1. Normal and abnormal spinal curvature [4]

The Cobb angle is the primary basis for determining the degree and symmetry of scoliosis in clinical practice. Its angles are generated by two tangent lines on the most tilted upper and lower relevant vertebrae's endplates [5], as shown in Figure 2 - the bigger the value, the greater the severity. The spine's deformity is categorized as mild when the angle is between 10 to 20 degrees; moderate in the range of 20 to 40; and severe if it exceeds 40. Table 1 shows the classifications.

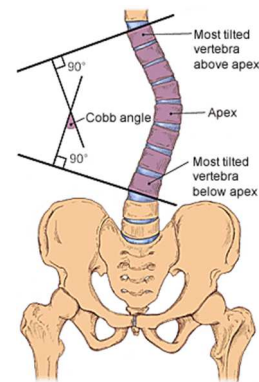


Fig. 2. Cobb angle measurement with reference lines [6]

TABLE 1
ACCEPTED CLINICAL COBB ANGLE SCOLIOSIS CATEGORY

Angle (in degrees)	Category
0 to 10	Normal spine
Between 10 to 20	Mild scoliosis
Between 20 to 40	Moderate scoliosis
Greater than 40	Severe scoliosis

Commission on Higher Education (CHED) – Institutional Development and Innovation Grants (IDIG)

978-1-6654-8453-4/22/\$31.00 ©2022 IEEE

Traditional image analysis for scoliosis diagnosis is a time-consuming and mechanical approach based on feature extraction. Physicians perform manual measurements, assessments, and identifications of specific vertebrae that present several challenges [7]. The fundamental problem is the anatomical variance across patients, and the poor tissue contrasts in spinal X-ray scans, making it difficult to precisely and dependably quantify the extent of the abnormalities. Moreover, instrumentation, vertebral movements, and patient's posture and positioning contribute to measurement error in the clinical evaluation of scoliosis. Experts observed around 2.8 to 8-degree variations in manual annotations of Cobb angle [8]. Artificial intelligence (AI) has vast potential for finding strong links within data [9 – 11] that can benefit medical diagnosis to predict the outcomes of clinical conditions. AI is paving the direction for improved healthcare by unlocking biological databases and datasets opportunities. As part of the industry 4.0 revolutions, it can assist with early, fast, and efficient diagnosis of X-ray, magnetic resonance, and computer tomography scans to ensure signs of illnesses are not overlooked.

Even though various methods for vertebral segmentation and scoliosis measurement are currently available, the literature indicates these researches are still in their infancy. The majority of solutions are mechanical [12], have constrained parameters [13], patched-based approaches losing contextual information [12] [14], and are restricted in their application by failing to consider the necessary individual vertebrae [15]. An article published by [16] employed a minimum bounding box patched-wise vertebral segmentation. Authors [17] applied K-means for curvature fitting approach requiring several preprocessing procedures, while searching for vertebrae corners using regression technique was proposed by [18]. Considering AI's potential, these supervised methods are less effective for medical applications due to their poor accuracy, caused by the loss of detailed information during the process and lack of interpretation.

Our research differs from previous studies by minimizing physical intervention and tedious pre and post-processing. The most significant contribution of this work is the development of an accurate end-to-end approach for scoliosis severity detection based on machine learning in aiding the medical industry in terms of rapid and reliable diagnosis.

II. METHODOLOGY

The following section discusses the detailed procedures to automatically acquire the angle measurement such as data acquisition and processing, spine isolation, vertebrae segmentation, severity classification, and performance evaluation.

A. Experimental Data Acquisition

We obtained 210 gray-scaled two-dimensional (2D) spinal X-ray images exhibiting scoliosis in the anterior-posterior (AP) view with a 1920 x 1080 pixels resolution from different image repositories (both open and non-open sources). Any forms of identification were removed per the country's data privacy law. Image enhancement or modification procedures

were skipped to preserve the images' true integrity, preventing unusual results. Samples include a complete picture of the thoracic and lumbar vertebrae, which is required for the intended image processing. A total of 180 training sets, 20 test sets, and 10 validation sets were selected purposively. All data are annotated with the expert's measurements of the Cobb angle for comparison between the traditional methods against the performance of machine learning algorithms.

B. Spinal Region Identification

The region of interest (ROI) identification method is critical for successful image processing since it aids in reducing and eliminating considerable amounts of noise. We reduced the size of all spinal anatomical projections to around 27.75% of their original dimensions, focusing exclusively on the thoracic and lumbar vertebrae that are most affected by scoliosis [19]. The task was accomplished using an aggregated channel feature (ACF) with LUV, which extracts features directly as pixel values from various color channels (gradient magnitudes), precisely its intensity values. Another reason to use the scheme is that it offers clear advantages like richer representation, faster detection speed, and accurate object localization [20]. We then utilized an Adaptive Boost (AdaBoost) algorithm to train the spine ACF to a cascade classifier. Finally, the last stage ends with a cropping operation on the recognized spine ROI in preparation for vertebral segmentation. Figure 3 shows the operational process flow.

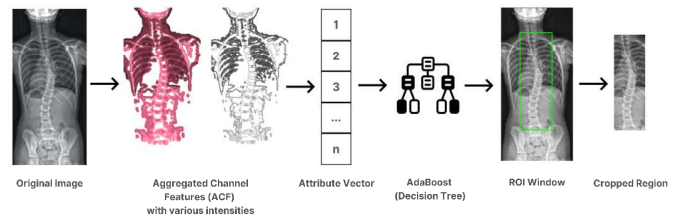


Fig. 3. Processing for spine region detection and isolation

C. Spine Boundary Identification

Following the isolation of the spine region, we used the ROI image to identify the location of the vertebrae in the spine. Overall, the spine appears with greater intensity, and we determine the spine's edges through the sums of the intensity and gradient values using color channel filters. The first step is to locate a vertebral segment to form a center segment line (CSL). A series of rectangle windows with height (H) and width (W) pixels are superimposed from left to right positioned along the apex of the spine's region, with one-pixel increments. The total luminance within each rectangular window was computed to derive the initial reference point for the CSL illustrated in Figure 4(a). Afterward, the existing rectangular frame with the highest intensity is pushed down a specific pixel (p). A search is launched for the next active point between identified pixels on each side (q). Similar repeated operations were carried out until multiple (r) reference points were identified, after which they were fitted into CSL using a polynomial fitting technique depicted in Figure 4(b) [21].

We then employed small window sections (10 x 4 pixels) to discover the delineation points of the spine in a specific direction by traversing pixels (x) on the target CSL point shown in Figure 4(c). When the disparity in intensity between the window frames is at its greatest, the midpoint part is chosen as the boundary point of the spine. The process for boundary recognition is repeated until all possible touchpoints (r) on the CSL are examined.

A reconstruction of the current matching window of the endpoint for the CSL is performed to complete successive detection until all spine limits are identified. Once the procedures are completed, a four-degree polynomial fitting for each side of the spinal boundary is fitted (see Figure 4(d)). For the spinal edges identification, we set the hyperparameters with the following values: $r = 4$, $x = 35$, $q = 10$, $p = 11$, $H = 50$ and $W = 12$.

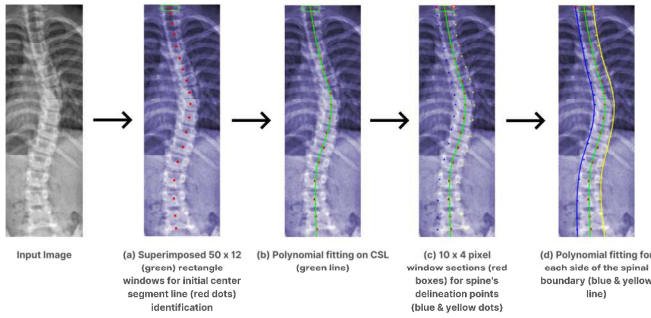


Fig. 4. Spine boundary identification process

D. Vertebrae Identification

Once the spine's edges are defined, we placed a midpoint line (ML) based on the edges shown in Figure 5(a) to isolate the spine's foreground region in Figure 5(b). These steps are crucial for vertebrae detection using three equally subspace lines depicted in Figures 5(c) and 5(d) to produce threshold images and values. We also observed higher luminance in the vertebrae areas and the histogram's image projection (p_i) summed up using Equation 1 [21]:

$$f_t(y) = \begin{cases} 0, & \text{if } p_t(y) > 0 \\ 1, & \text{opposite,} \end{cases} \quad (1)$$

Where y is the histogram's index, B is the ML's length, and B is also the bin dimension of histogram p_t . The cumulative histogram P is the subtotals of each f_i on Equation 2 [21]:

$$P(y) = \sum_{i=1}^n f_t(y) \quad (2)$$

The contiguous pixels of the disc are partaking in the computation of histogram P through a voting method where most vertebrae's value is 0. Meanwhile, the ROI for a vertebra was obtained by selecting each profound shift in ascending order of histogram P as a starting point. We then created an 18 bin non-overlapped sub-histogram from the histogram commencing with the lower bound vertebra to derive the final

vertebral ROI surrounded by adjoining lines. The vertebrae's initial boundaries are presented in Figure 5(e).

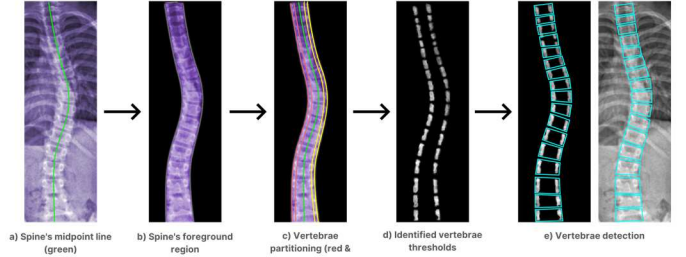


Fig. 5. Vertebrae identification process

E. Vertebrae Segmentation

Following the vertebrae identification procedure, we extracted ROI from each spine image. However, the intensity of the vertebrae in the spine's AP view varies significantly. The cervical portion appears to be of lower intensity, while the lumbar is high. Existing convolutional neural network (CNN) algorithms, as a by-product, have evolved into an essential alternative for dealing with the problem of intensity inconsistency.

To solve these occurrences and as illustrated in Figure 6, we altered the standard U-Net architecture [22] to make it more suitable for our segmentation purposes. The encoder portion (left side) uses convolution and downsampling to collect information from the input image and store it in feature maps. A prediction map is reconstructed by the decoder section (right side) using upsampling and concatenation. Moreover, in the original U-Net's design, critical information is lost due to cropping – a significant drawback. As a solution, we substituted a concatenation procedure based on similar strategies by [21] [23], and a 256 x 128 vertebra ROI was fed into the network for segmentation.

In our experiment, we imposed a 3 x 3 stride 1 to filter in the convolution layers with a rectified linear unit (RELU) and normalization applied to both network parts (encoder & decoder) to extract the image's features. A RELU is an activation function that allows for nonlinear reshaping of the feature map at a low computational cost and improved efficiency [24]. We then executed downsampling to shrink the feature map's size using max-pooling (2 x 2 with second-degree stride) to make learned features highly robust and diminish noise.

During upsampling, a decoder branch deconvolutes and normalizes the feature maps, reducing the feature channels using a 3 x 3 filter size convolution. Afterward, the output is linked with the encoder part's corresponding feature maps. The last layer applied a 1 x 1 filter convolution to convert the feature map into 64 channels between 0 and 1 for segmentation thresholds. We benchmarked different network frameworks based on a standard U-Net, Residual U-Net, and Dense U-Net [22]. The residual design (Figure 6) differs from a conventional U-Net in that a standard convolution operation substitutes the block implementation to alleviate the network's deterioration issues as the layer increases [25]. Each residual block comprises repeated procedures, including batch

normalization, RELU activation function, and a 3 x 3 filter convolution.

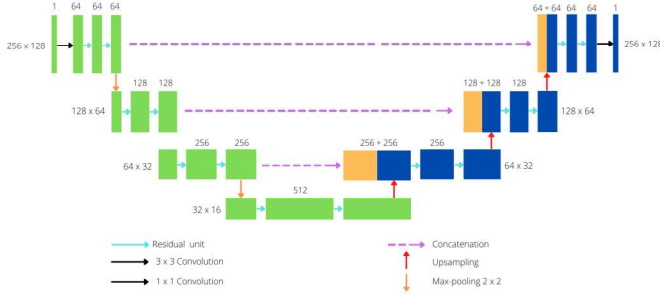


Fig. 6. Residual U-Net architecture for vertebrae segmentation

On the other hand, a Dense U-Net is created on top of a Residual U-Net, with each block layer acquiring identification maps from all preceding layers. Furthermore, it preserves prior layer features and considerably enhances gradient propagation via integrated channel-wise concatenation. This mechanism preserves information between layers, leading to higher precision and fewer computations. The structure is appropriate for medical imaging analyses in which objects frequently overlap, such as brain tumors, pneumonia, blood vessel segmentation, liver cancer, and multi-organ segmentation. To assess the segmentation performance of each model, we employed 10-fold cross-validation. An ADAM optimizer trains all CNN network with hyperparameters of learning rate initial value = 0.01, epochs = 100, batch size = 10, and dropout rate = 0.25. At the same time, a sum of the squares of the differences between the ground truth and prediction were minimized using an L2-norm loss function for optimization [26].

F. Cobb Angle Calculation

To quantify the Cobb angle automatically, we devised a minimum bounding box (MBB) method to identify the vertebrae's upper and lower border through segmented contours ($max\ x$, $max\ y$, $min\ x$, & $min\ y$) shown in Figure 7.

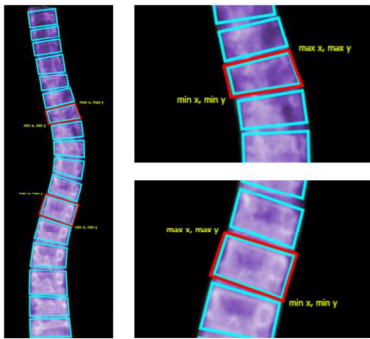


Fig. 7. MBB for detecting vertebra's upper and lower border

Once the specific borders are defined, all the vertebrae's endplate angles are estimated and stored in an array to determine the two most tilted vertebrae in the upper and lower part of the spine (Figure 2). After referencing specific vertebrae, the curvature angle (C_s) is then calculated for the spine represented by Equation 3:

$$C_s = \max \left\{ \left| \tan^{-1} \left(\frac{x_i - x_j}{1 + x_i - x_j} \right) \right| \right\} \quad (3)$$

Where x_i is the slope of the upper vertebrae's upper border and x_j is the slope of the lower vertebrae's lower edge.

G. Segmentation Performance Metrics

We evaluated the segmentation results using dice similarity coefficient (DSC), Jaccard similarity (JS), and mean squared error (MSE). DSC is a popular semantic validation technique in AI measured in terms of overlap scope by two segmentations divided by the total size of the two objects [27][28] expressed by Equation 4:

$$DSC = \frac{2|GT \cap PS|}{|GT| + |PS|} \quad (4)$$

JS is also a standard performance metric because of its straightforward, practical approach [30]. It quantifies the overlap between predicted segmentation (PS) and the actual or ground truth (GT) divided by the union area between the PS and the GT . Both metrics range from 0 to 1, with 0 signifying no overlap and 1 indicating a perfect segmentation [28]. The computed JS is represented by Equation 5:

$$JS = \frac{|GT \cap PS|}{|GT \cup PS|} \quad (5)$$

Finally, MSE is the simplest reference metric calculated by the squared differences between image segmentation [29] from GT and PS summarized by Equation 6:

$$MSE = \frac{1}{n} \sum_{i=1}^n (GT_i - PS_i)^2 \quad (6)$$

H. Spine Curvature Evaluation Metrics

For this study, we compared the medical doctor's Cobb angle measurement (manual) results against our artificial intelligence-based automatic approach. A T-test statistical parametric approach was performed due to the normal distribution of the validation set to identify a significant difference between the means of two (independent) groups [30]. The configurations are set at 95% confidence interval and a p-value of 0.05. A value less than the set p-value threshold signal a statistically significant difference while the opposite tells otherwise. The formula for the test is expressed by Equation 7:

$$t = \frac{\bar{x}_1 - \bar{x}_2}{s_p \sqrt{\frac{1}{n_1} + \frac{1}{n_2}}} \quad (7)$$

Where \bar{x}_1 and \bar{x}_2 are the mean of the first and second sample, n_1 and n_2 are the size of observations of both samples, and s_p is the pooled standard deviation. Furthermore, the reliability of the angle measurement by our proposed methods was assessed through mean absolute percentage error (MAPE), a popular non scale-dependent measure for forecasting non-extreme or non-zero value data depicted by Equation 8:

$$MAPE = \frac{\sum_{i=1}^N \left| \frac{o_i - p_i}{p_i} \right| \times 100}{N} \quad (8)$$

Where o_i is the observed value, p_i is the predicted value, and N is the number of samples.

III. RESULTS

We performed the experiments using a personal computer (PC) with a Core i7 (4.60 GHz, 24M cache) processor, 32 GB random access memory (RAM), and an NVIDIA GEFORCE RTX 3070 GPU (1.73 GHz, 16 GB) dedicated graphics card. Our neural network's constructions were executed based on Python's Tensorflow library. The following subsections detail the results.

A. Segmentation Evaluation Results

Table 2 shows the DSC, JS, and MSE from cross-validation of different convolutional network models, including training and test execution times. Based from the results, Residual U-Net perform better (0.951, 0.908 & 0.025) than the U-Net (0.942, 0.890 & 0.032), and the Dense U-net (0.946, 0.901 & 0.027). The results confirmed that a residual unit helps when training deep architectures for better image analysis representation [31 – 33]. Figure 8 shows an excerpt of the three network's vertebrae segmentations pitted against the ground truth.

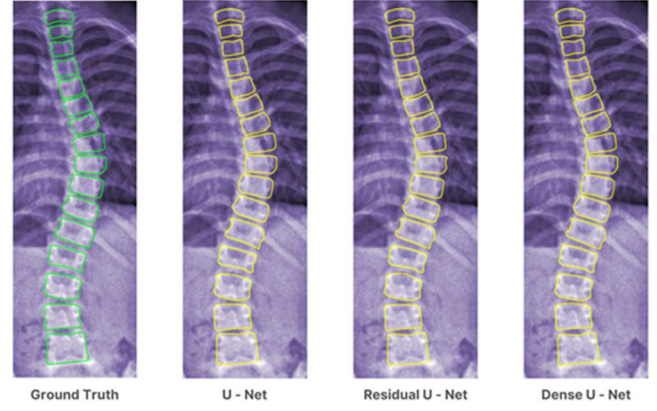


Fig. 8. Comparative segmentation results of the three networks

B. Top and Bottom Vertebrae Reference Evaluation

We also compared the deviations between the experts' judgment against the predicted vertebrae references in Table 3 that are crucial for the accurate measurements of the Cobb angle. Based on the results, our machine learning methods, on average, deviate only with a small margin of error of 0.60 and 0.50 for top and bottom vertebrae – this is an improvement from the work of [34]. Moreover, we also observed that lower vertebrae referencing is easier to identify because of the X-ray images' apparent high luminance on the lumbar part with less intermingling features than the thoracic portions of the spine.

TABLE 2

DICE & JACCARD SIMILARITY COEFFICIENTS, AND MEAN SQUARED ERROR SEGMENTATION EVALUATION OF EACH NEURAL NETWORK

k-fold	Dice similarity coefficient (DSC)			Jaccard similarity index (JS)			Mean squared error (MSE)		
	U-Net	Residual U-Net	Dense U-Net	U-Net	Residual U-Net	Dense U-Net	U-Net	Residual U-Net	Dense U-Net
1	0.943 ± 0.035	0.953 ± 0.024	0.947 ± 0.028	0.891 ± 0.053	0.909 ± 0.046	0.902 ± 0.043	0.030 ± 0.016	0.024 ± 0.013	0.027 ± 0.017
2	0.942 ± 0.033	0.952 ± 0.023	0.945 ± 0.027	0.890 ± 0.048	0.910 ± 0.044	0.900 ± 0.044	0.031 ± 0.014	0.025 ± 0.012	0.028 ± 0.016
3	0.942 ± 0.031	0.951 ± 0.028	0.943 ± 0.029	0.889 ± 0.049	0.908 ± 0.043	0.901 ± 0.046	0.032 ± 0.015	0.023 ± 0.011	0.026 ± 0.015
4	0.941 ± 0.032	0.950 ± 0.025	0.945 ± 0.030	0.891 ± 0.047	0.907 ± 0.041	0.904 ± 0.043	0.033 ± 0.018	0.024 ± 0.014	0.027 ± 0.018
5	0.943 ± 0.034	0.951 ± 0.026	0.946 ± 0.031	0.892 ± 0.048	0.911 ± 0.039	0.903 ± 0.042	0.031 ± 0.017	0.026 ± 0.015	0.029 ± 0.019
6	0.941 ± 0.033	0.949 ± 0.027	0.947 ± 0.030	0.891 ± 0.051	0.910 ± 0.040	0.902 ± 0.044	0.032 ± 0.014	0.027 ± 0.011	0.028 ± 0.015
7	0.944 ± 0.031	0.952 ± 0.028	0.948 ± 0.029	0.889 ± 0.045	0.908 ± 0.041	0.901 ± 0.043	0.033 ± 0.015	0.028 ± 0.012	0.027 ± 0.014
8	0.945 ± 0.033	0.953 ± 0.029	0.946 ± 0.028	0.892 ± 0.048	0.909 ± 0.039	0.901 ± 0.045	0.034 ± 0.016	0.026 ± 0.013	0.029 ± 0.016
9	0.943 ± 0.036	0.952 ± 0.027	0.947 ± 0.027	0.891 ± 0.050	0.908 ± 0.042	0.903 ± 0.046	0.032 ± 0.017	0.025 ± 0.014	0.028 ± 0.017
10	0.943 ± 0.035	0.953 ± 0.028	0.946 ± 0.025	0.889 ± 0.049	0.909 ± 0.044	0.902 ± 0.042	0.033 ± 0.018	0.026 ± 0.012	0.029 ± 0.015
Average ± std	0.942 ± 0.033	0.951 ± 0.026	0.946 ± 0.028	0.890 ± 0.048	0.908 ± 0.041	0.901 ± 0.043	0.032 ± 0.016	0.025 ± 0.012	0.027 ± 0.016
a. Training time: U-Net (25.42 minutes), Residual U-Net (30.24 minutes), and Dense U-Net (51.35 minutes)									
b. Testing time: U-Net (0.02 seconds), Residual U-Net (0.04 seconds), and Dense U-Net (0.06 seconds)									

TABLE 3

PERFORMANCE TEST OF THE DEEP LEARNING METHOD VS. MEDICAL EXPERT'S MEASUREMENTS

Validation ID	Medical expert's measurements (Ground truth)			Deep learning measurements (Prediction)			Absolute difference (Ground truth vs. Prediction)		
	Top vertebrae	Bottom vertebrae	Cobb angle (in degrees)	Top vertebrae	Bottom vertebrae	Cobb angle (in degrees)	Top vertebrae	Bottom vertebrae	Cobb angle (in degrees)
001	T09	L02	22.90	T10	L03	19.78	1	1	3.12
002	T10	L03	10.50	T09	L03	7.93	1	0	2.57
003	T10	L04	14.86	T11	L04	13.21	1	0	1.65
004	T06	T11	26.42	T06	T10	27.85	0	1	1.43
005	T05	T12	21.51	T06	T12	24.42	1	0	2.91
006	T11	L03	21.36	T11	L03	20.89	0	0	0.47
007	T07	L03	41.69	T08	L04	39.73	1	1	1.96
008	T07	T11	30.56	T07	T11	29.75	0	0	0.81
009	T06	L03	42.15	T05	L02	41.85	1	1	0.30
010	T05	T11	15.79	T05	T12	16.34	0	1	0.55
a. Vertebrae legend: T11 – T12 (thoracic), L01 – L05 (lumbar) [1]									
b. T-test (Ground truth vs. Predicted Cobb angle): $t = 0.1237$, degree of freedom (df) = 18, p-value = 0.9028									
c. MAPE (Ground truth vs. Predicted Cobb angle): 8.18% (Accuracy = 91.81%)									
d. Mean difference (Ground truth vs. Predicted Cobb angle): 1.57 degrees									
e. Mean difference (Expert vs. Prediction reference for top vertebrae): 0.60									
f. Mean difference (Expert vs. Prediction reference for bottom vertebrae): 0.50									

C. Cobb Angle Evaluation Results

For the evaluation of scoliosis, we compare the performance of the Residual U-Net's model against the reference measurement obtained from the medical experts. Table 3 reports the comparative results between manual measurements versus our deep learning approach. Based on the T-test results, there is no significant difference between the two sets of measurements ($p\text{-value} = 0.9028$, $t = 0.1237$) and a MAPE of 8.18%. This shows that our approach is relatively closer to actual observed values by medical experts with an acceptable mean absolute difference of 1.57 degrees [8]. Figure 9 shows a visual computation from reference lines.

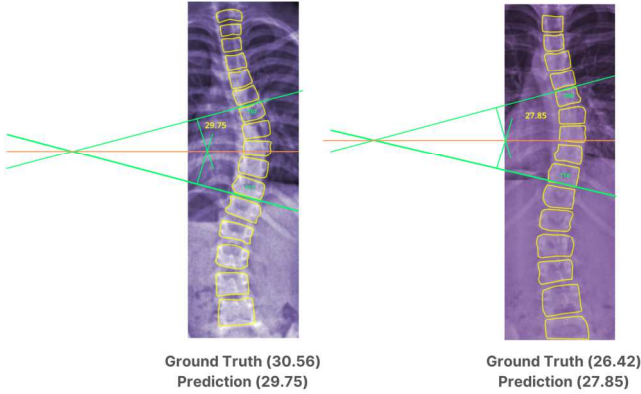


Fig. 9. Automatic Cobb angle measurement (Ground Truth vs. Prediction)

IV. DISCUSSIONS

This research established that our approach could automatically measure the Cobb angle to define the scoliosis severity using various intuitive procedures. The empirical results indicated that the Residual U-Net surpasses both the U-Net and Dense U-Net networks in recognizing the internal and external vertebral structures, with a mean segmentation accuracy of 92.95% for DSC and JS. Moreover, the residual network decreases segmentation error by 0.975% - a substantial improvement rate in image processing. Our tests demonstrated that comprehensive and optimized procedures such as spinal region isolation, spine boundary identification, vertebrae detection and segmentation served as a prelude to accurate Cobb angle measurements with a precision of 91.81% via MAPE. While optimization for each stage was a computationally intensive and time-consuming endeavor, the gains outweighed the drawbacks. Additionally, the pipeline's robustness validation was confirmed by medical experts' observed Cobb angle measurements over our machine learning methods with a T-test $p\text{-value}$ of 0.9028. It suggests that there are no significant differences between the calculations of the two groups. This work also noted that complex architecture such as Dense U-Net did not necessarily lead to accurate segmentation. Each framework has its specific strengths and weaknesses depending on its application [22]. Our findings are at par with the research of [12 - 17] [21] [35 - 37] in artificial intelligence-based medical image processing. Like any research, we have encountered the challenges of noisy X-ray scans due to insufficient image quality and patient's

unbalanced posture contributing to forecast deviations of the Cobb angle measurement. This study did not explore algorithms for compensating these issues, such as image reconstructions, enhancements, and reorientation corrections.

V. CONCLUSIONS AND FUTURE WORK

Scoliosis is a spinal abnormality that causes a multitude of short-term to long-term health-related problems such as posture deformity, nerve pains, balance issues, osteoarthritis, degenerative diseases, and internal organ damage. An accurate prognosis of its curvature severity is crucial for medical practitioners' treatment planning decisions. Traditional methods of Cobb angle measurement is an arduous and time-consuming manual process that is susceptible to discrepancies associated with a physician's subjective experience, perception, and expertise of each case. In addition, manual vertebrae segmentation and referencing prove to be troublesome to use only the naked eye. X-ray images are noisy because of their overlapping features (bones, lungs, heart, etc.).

We proposed a systematic pipeline for automatic Cobb angle measurement using deep learning based on Residual U-Net convolutional architecture to solve this predicament. Our experimental results demonstrated high accuracy and consistency between the annotated expert's measurements versus our automatic quantification with an acceptable mean deviation of only 1.57 degrees – a reliable value less than the standard manual variations. We contributed to the body of knowledge in advancing machine-driven medical imaging analysis by producing a dependable yet simplified scoliosis severity identification using artificial intelligence. Our framework can assist doctors in clinical practice to better understand scoliosis and its complementary treatments. The authors plan to improve the model's accuracy for future work by increasing the number of training sets, a better segmentation algorithm, and evaluating other convolutional neural networks' performances.

ACKNOWLEDGEMENT

The lead-author would like to thank the Commission on Higher Education (CHED) and Southern Luzon State University (SLSU) for supporting and funding this research through the institutional development and innovation grants (IDIG), including all contributors from different higher education institutions (HEIs).

REFERENCES

- [1] Vertebrae column, Accessed: January 15, 2022, [Online], Available: <https://www.britannica.com/science/vertebra/>
- [2] F. R. Labrom, M. T. Izatt, A. P. Claus, and J. P. Little, "Adolescent idiopathic scoliosis 3D vertebral morphology, progression and nomenclature: A current concepts review", *European Spine Journal*, 30(7), pp. 1823-1834, 2021.
- [3] J. McAviney, C. Roberts, B. Sullivan, A. J. Alevras, P. L. Graham and B. T. Brown, "The prevalence of adult de novo scoliosis: A systematic review and meta-analysis", *European Spine Journal*, 29(12), pp. 2960-2969, 2020.

- [4] Scoliosis, HH Publishing, Accessed: January 17, 2022, [Online], Available: https://www.health.harvard.edu/a_to_z/scoliosis-a-to-z
- [5] X. Fu, G. Yang, K. Zhang, N. Xu and J. Wu, "An automated estimator for Cobb angle measurement using multi-task networks", *Neural Computing and Applications*, 33(10), pp. 4755-4761, 2021.
- [6] K. A. Greiner, "Adolescent idiopathic scoliosis: Radiologic decision-making", *American Family Physician*, 65(9), pp. 1817-1822, 2002.
- [7] A. K. Al-Bashir, M. A. Al-Abed, H. K. Amari, F. M. Al-Rousan, O. M. Bashmaf, E. W. Abdulhay et al., "Computer-based Cobb angle measurement using deflection points in adolescence idiopathic scoliosis from radiographic images", *Neural Computing and Applications*, 31(5), pp. 1547-1561, 2019.
- [8] Y. Sun, Y. Xing, Z. Zhao, X. Meng, G. Xu and Y. Hai, "Comparison of manual versus automated measurement of Cobb angle in idiopathic scoliosis based on a deep learning keypoint detection technology", *European Spine Journal*, 2021.
- [9] R. R. Maaliw, K. A. Quing, A. C. Lagman, B. H. Ugalde, M. A. Ballera and M. A. D. Ligayo, "Employability prediction of engineering graduates using ensemble classification modeling", 2022 IEEE 12th Annual Computing and Communication Workshop and Conference (CCWC), pp. 288-294, 2022.
- [10] R. R. Maaliw, "A personalized virtual learning environment using multiple modeling techniques", 2021 IEEE 12th Annual Ubiquitous Computing, Electronics & Mobile Communication Conference (UEMCON), pp. 8-15, 2021.
- [11] R. R. Maaliw, "Early prediction of electronics engineering licensure examination performance using random forest", 2021 IEEE World Artificial Intelligence & Internet of Things Congress (AIIoT), pp. 41-47, 2021.
- [12] Y. Tu, N. Wang, F. Tong and H. Chen, "Automatic measurement algorithm of scoliosis Cobb angle based on deep learning", *Journal of Physics: Conference Series*, 1187(4), p. 4210, 2019.
- [13] O. A. Okashi, H. Du, and H. Al-Assam, "Automatic spine curvature estimation from X-ray images of a mouse model", *Computer Methods and Programs in Biomedicine*, vol. 140, pp. 175-184, 2017.
- [14] R. H. Alharbi, M. B. Alshaye, M. M. Alkanhal, N. M. Alharbi, M. A. Alzahrani and O. A. Alrehaili, "Deep learning based algorithm for automatic scoliosis angle measurement", 2020 IEEE 3rd International Conference on Computer Applications & Information Security (ICCAIS), pp. 1-5, 2020.
- [15] K. Zhang, N. Xu, G. Yang, J. Wu, and X. Fu, "An automated cobb angle estimation method using convolutional neural network with area limitation", 2019 International Conference on Medical Image Computing and Computer-Assisted Intervention, pp. 775-783, 2019.
- [16] C. Huang, H. Tang, W. Fan, K. Cheung, M. To, Z. Qian and D. Terzopoulos, "Fully-automated analysis of scoliosis from spinal X-ray images", 2020 IEEE 33rd International Symposium on Computer-Based Medical Systems (CBMS), pp. 114-119, 2019.
- [17] S. Pasha and J. Flynn, "Data-driven classification of the 3D spinal curve in adolescent idiopathic scoliosis with an applications in surgical outcome prediction", *Scientific Reports*, 8(1), pp. 1-10, 2018.
- [18] E. García-Cano, F. A. Cosío, L. Duong, C. Bellefleur, M. Roy-Beaudry et al., "Prediction of spinal curve progression in adolescent idiopathic scoliosis using random forest regression", *Computers in Biology and Medicine*, vol. 103, pp. 34-43, 2018.
- [19] C. R. Fischer, L. G. Lenke, K. H. Bridwell, O. Boachie-Adjei, M. Gupta, and Y. J. Kim, "Optimal lowest instrumented vertebra for thoracic adolescent idiopathic scoliosis", *Spine Deformity*, 6(3), pp. 250-256, 2018.
- [20] F. A. Hermawati, H. Tjandrasa and N. Suciati, "Combination of aggregated channel features (ACF) detector and Faster R-CNN to improve object detection performance in fetal ultrasound images", *International Journal of Intelligent Engineering Systems*, 11(6), pp. 1-10, 2018.
- [21] M. H. Horng, C. P. Kuok, M. J. Fu, C. J. Lin and Y. N. Sun, "Cobb angle measurement of spine from X-ray images using convolutional neural network", *Computational and Mathematical Methods in Medicine*, pp. 1-19, 2019.
- [22] N. Siddique, S. Paheding, C. P. Elkin and V. Devabhaktuni, "U-net and its variants for medical image segmentation: A review of theory and applications", *IEEE Access*, volume 9, pp. 82031-82057, 2021.
- [23] N. Sambyal, P. Saini, R. Syal and V. Gupta, "Modified U-Net architecture for semantic segmentation of diabetic retinopathy images", *Biocybernetics and Biomedical Engineering*, 40(3), pp. 1094-1109, 2020.
- [24] Y. D. Zhang, C. Pan, X. Chen and F. Wang, "Abnormal breast identification by nine-layer convolutional neural network with parametric rectified linear unit and rank-based stochastic pooling", *Journal of Computational Science*, vol. 27, pp. 57-68, 2018.
- [25] M. Z. Alom, C. Yakopcic, M. Hasan, T. M. Taha and V. K. Asari, "Recurrent residual U-Net for medical image segmentation", *Journal of Medical Imaging*, 6(1), 2019.
- [26] J. Cao, Z. Su, L. Yu, D. Chang, X. Li and Z. Ma, "Softmax cross entropy loss with unbiased decision boundary for image classification", 2018 IEEE Chinese Automation Congress (CAC), pp. 2028-2032, 2018.
- [27] R. Robinson, O. Oktay, W. Bai, V. V. Valindria, M. M. Sanghvi, N. Aung et al., "Real-time prediction of segmentation quality", *International Conference on Medical Image Computing and Computer-Assisted Intervention*, pp. 578-585, 2018.
- [28] T. Eelbode, J. Bertels, M. Berman, D. Vandermeulen, F. Maes, R. Bisschops and M. B. Blaschko, "Optimization for medical image segmentation: Theory and practice when evaluating with dice score or jaccard index", *IEEE Transactions on Medical Imaging*, 39(11), pp. 3679-3690, 2020.
- [29] R. R. Maaliw, M. A. Ballera, Z. P. Mabunga, A. T. Mahusay, D. A. Dejelo and M. P. Seño, "An ensemble machine learning approach for time series forecasting of COVID-19 cases", 2021 IEEE 12th Annual Information Technology, Electronics and Mobile Communication Conference (IEMCON), pp. 633-640, 2021.
- [30] B. Gerald, "A brief review of independent, dependent and one sample t-test", *International Journal of Applied Mathematics and Theoretical Physics*, 4(2), pp. 50-54, 2018.
- [31] Z. Zhang, Q. Liu and Y. Wang, "Road extraction by deep residual u-net", *IEEE Geoscience and Remote Sensing Letters*, 15(5), pp. 749-753, 2018.
- [32] A. Khanna, N. D. Londhe, S. Gupta and A. Semwal, "A deep residual u-net convolutional neural network for automated lung segmentation in computed tomography images", *Biocybernetics and Biomedical Engineering*, 40(3), pp. 1314-1327, 2020.
- [33] D. Li, D. A. Dharmawan, B. P. Ng and S. Rahardja, "Residual u-net for retinal vessel segmentation", 2019 IEEE International Conference on Image Processing (ICIP), pp. 1425-1429, 2019.
- [34] N. A. Makhdoomi, T. S. Gunawan, N. H. Idris, O. O. Khalifa, R. K. Karupiah et al., "Development of Scoliotic Spine Severity Detection using Deep Learning Algorithms", 2022 IEEE 12th Annual Computing and Communication Workshop and Conference (CCWC), pp. 0574-0579, 2022.
- [35] W. Caesarendra, W. Rahmiani, J. Mathew and A. Thien, "Automated Cobb angle measurement for adolescent idiopathic scoliosis using convolutional neural network", *Diagnostics*, 12(2), 2022.
- [36] B. Khanal, L. Dahal, P. Adhikari and B. Khanal, "Automatic cobb angle detection using vertebra detector and vertebra corners regression", *International Workshop and Challenge on Computational Methods and Clinical Applications for Spine Imaging*, pp. 81-87, 2019.
- [37] Y. Pan, Q. Chen, T. Chen, H. Wang, X. Zhu, Z. Fang and Y. Lu, "Evaluation of a computer-aided method for measuring the Cobb angle on chest X-rays", *European Spine Journal*, 28(12), pp. 3035-3043, 2019.